A direct calibration of thtae IRX-β relation in Lyman-break Galaxies at z = 3-5

(article starts on next page)

A direct calibration of the IRX–β relation in Lyman-break Galaxies at z = 3–5

M. P. Koprowski,[1]★ K. E. K. Coppin,[1] J. E. Geach,[1] R. J. McLure,[2] O. Almaini,[3]
A. W. Blain,[4] M. Bremer,[5] N. Bourne,[2] S. C. Chapman,[6] C. J. Conselice,[7]
J. S. Dunlop,[2] D. Farrah,[8] W. Hartley,[9] A. Karim,[10] K. K. Knudsen,[11]
M. J. Michałowski,[12] D. Scott,[13] C. Simpson,[14] D. J. B. Smith[1] and
P. P. van der Werf[15]

[1]*Centre for Astrophysics Research, School of Physics, Astronomy and Mathematics, University of Hertfordshire, College Lane, Hatfield AL10 9AB, UK*
[2]*Institute for Astronomy, University of Edinburgh, Royal Observatory, Edinburgh EH9 3HJ, UK*
[3]*School of Physics and Astronomy, University of Nottingham, University Park, Nottingham NG7 2RD, UK*
[4]*Physics & Astronomy, University of Leicester, 1 University Road, Leicester LE1 7RH, UK*
[5]*Astrophysics Group, School of Physics, University of Bristol, Tyndall Avenue, Bristol BS8 1TL, UK*
[6]*Department of Physics and Atmospheric Science, Dalhousie University, Halifax NS B3H 4R2, Canada*
[7]*University of Nottingham, School of Physics & Astronomy, Nottingham NG7 2RD, UK*
[8]*Department of Physics, Virginia Tech, Blacksburg, VA 24061, USA*
[9]*Department of Physics and Astronomy, University College London, London WC1E 6BT, UK*
[10]*Argelander-Institut für Astronomie, Universität Bonn, Auf dem Hügel 71, D-53121 Bonn, Germany*
[11]*Department of Space, Earth and Environment, Chalmers University of Technology, Onsala Space Observatory, SE-43992 Onsala, Sweden*
[12]*Astronomical Observatory Institute, Faculty of Physics, Adam Mickiewicz University, ul. Słoneczna 36, 60-286 Poznań, Poland*
[13]*Department of Physics and Astronomy, 6224 Agricultural Road, University of British Columbia, Vancouver V6T 1Z1, Canada*
[14]*Gemini Observatory, Northern Operations Center, 670 N. A'ohuku Place, Hilo, HI 96720, USA*
[15]*Leiden Observatory, Leiden University, P.O. Box 9513, NL-2300 RA Leiden, the Netherlands*

ABSTRACT

We use a sample of 4209 Lyman-break galaxies (LBGs) at $z \simeq 3$, 4, and 5 in the UKIRT
Infrared Deep Sky Survey Ultra Deep Survey field to investigate the relationship between the
observed slope of the stellar continuum emission in the ultraviolet, β, and the thermal dust
emission, as quantified via the so-called 'infrared excess' (IRX $\equiv L_{\mathrm{IR}}/L_{\mathrm{UV}}$). Through a stacking
analysis, we directly measure the 850-μm flux density of LBGs in our deep (0.9 mJy) James
Clerk Maxwell Telescope *SCUBA-2* 850-μm map as well as deep public *Herschel*/SPIRE
250-, 350-, and 500-μm imaging. We establish functional forms for the IRX–β relation to
$z \sim 5$, confirming that there is no significant redshift evolution of the relation, and that the
resulting average IRX–β curve is consistent with a Calzetti-like attenuation law. Comparing
our results with recent works in the literature, we confirm that discrepancies in the slope of
the IRX–β relation are driven by biases in the methodology used to determine the ultraviolet
slopes. Consistent results are found when IRX–β is evaluated by stacking in bins of stellar
mass, and we argue that the near-linear IRX–$M_\star$ relationship is a better proxy for correcting
observed ultraviolet luminosities to total star formation rates, provided an accurate handle on
$M_\star$ and also gives clues as to the physical driver of the role of dust-obscured star formation in
high-redshift galaxies.

Key words: dust, extinction – galaxies: high-redshift – galaxies: ISM – galaxies: star forma-
tion – cosmology: observations.

1 INTRODUCTION

Understanding the evolution of the star formation rate density
(SFRD) with cosmic time has long been the cornerstone of ex-

★ E-mail: m.koprowski@herts.ac.uk

tragalactic astrophysics (e.g. Madau & Dickinson 2014). At $z > 2$, most studies of the evolution of the SFRD are based on samples of Lyman-break galaxies (LBGs), due in part because of the efficiency of their selection technique in deep broad-band imaging surveys.

As a result, LBGs have been extensively studied and well characterized over the past two decades. They have stellar masses $\sim 10^{9-11}$ M$_\odot$ and star formation rates (SFRs) $\sim 10-100$ M$_\odot$ yr^{-1} (e.g. Madau et al. 1996; Steidel et al. 1996; Sawicki & Yee 1998; Shapley et al. 2001; Giavalisco 2002; Blaizot et al. 2004; Shapley et al. 2005; Reddy et al. 2006; Rigopoulou et al. 2006; Verma et al. 2007; Magdis et al. 2008; Chapman & Casey 2009; Lo Faro et al. 2009; Stark et al. 2009; Magdis et al. 2010; Pentericci et al. 2010; Rigopoulou et al. 2010; Bian et al. 2013; Oteo et al. 2013). LBGs are therefore believed to be responsible for forming a substantial fraction of massive local galaxies ($L > L^*$; e.g. Somerville, Primack & Faber 2001; Baugh et al. 2005), while those with the highest SFRs (> 100 M$_\odot$ yr^{-1}) could be the progenitors of present-day ellipticals (e.g. Verma et al. 2007; Reddy & Steidel 2009; Stark et al. 2009).

Naturally, given their selection, the most common tracer of LBGs' SFRs has traditionally been through their rest-frame UV stellar continuum emission (e.g. Kennicutt & Evans 2012). However, it is now well known that about half of the starlight in the Universe is absorbed by interstellar dust and re-emitted in the rest-frame far-infrared (e.g. Dole et al. 2006). It is therefore necessary to complement UV-derived SFRs with far-infrared and sub-millimetre observations to obtain a full census of star formation, with the latter providing the most efficient probe of thermal dust emission out to high redshift owing to the negative k-correction. Unfortunately, typical LBGs are faint in the sub-millimetre, far below the confusion limit of most single-dish sub-millimetre facilities and challenging even for sensitive interferometric facilities such as the Atacama Large Millimeter/sub-millimeter Array (ALMA; Chapman et al. 2000; Capak et al. 2015; Bouwens et al. 2016; Koprowski et al. 2016; Dunlop et al. 2017; McLure et al. 2018). As a result, representative samples of sub-millimetre-detected LBGs are not available.

Without direct detection of the obscured star formation in individual LBGs, empirical recipes are used to correct UV-derived SFRs to total SFRs. The most common approach is to use the relationship between the rest-frame UV slope, β, where $f_\lambda \propto \lambda^\beta$, and the infrared excess, IRX $\equiv L_{\rm IR}/L_{\rm UV}$ (Meurer, Heckman & Calzetti 1999). Overzier et al. (2011) found that local analogues of LBGs are consistent with the Meurer et al. (1999) relation, while at $z \gtrsim 3$ Coppin et al. (2015) and Álvarez-Márquez et al. (2016) found LBGs to be lying above and below the local relation, respectively. Recently, McLure et al. (2018) showed that the IRX–β relation for $z \sim 3$ galaxies is consistent with a Calzetti-like attenuation law (Calzetti et al. 2000), while Reddy et al. (2018) suggest that a flatter, Small Magellanic Cloud (SMC)-like curve should be applied. In addition, a number of individual direct detections for LBGs and infrared-selected galaxies have been found to exhibit a large scatter in the IRX–β plane (e.g. Casey et al. 2014; Capak et al. 2015; Koprowski et al. 2016; Scoville et al. 2016; Fudamoto et al. 2017). It remains unclear whether these inconsistencies are due to intrinsic scatter in the IRX–β relation or biases in the selection and measurement techniques. It is therefore necessary to perform a critical analysis at these high redshifts, utilizing a large, unbiased sample of galaxies.

In this paper, we use 4209 LBGs at redshifts $3 < z < 5$ in the UKIRT Infrared Deep Sky Survey (UKIDSS)/Ultra-Deep Survey (UDS) field, stellar mass complete down to a limit of $\log(M_*/M_\odot) \gtrsim 10.0$, to establish the IRX–$\beta$ relation. We are able to determine the IR luminosities for these galaxies through stacking in a deep JCMT

SCUBA-2 850-µm map from the *SCUBA-2* Cosmology Legacy Survey (S2CLS; Geach et al. 2017), and 350–500 µm SPIRE mapping from the *Herschel Space Observatory*. This paper expands on the work of Coppin et al. (2015), with a $2 \times$ deeper *SCUBA-2* map of UDS, now approaching the *SCUBA-2* confusion limit (with a 1σ depth of 0.9 mJy beam^{-1}) as well as improved methodology for determining UV slopes and a clearer LBG sample. With this sample, we are able to calibrate the IRX–β relationship out to redshifts as high as $z \sim 5$ and therefore determine the average dust properties of star-forming galaxies, which are much less prone to selection biases characteristic of small samples at these early times (e.g. Capak et al. 2015). Section 2 summarizes the data used and explains our LBG selection criteria. In Section 3, we explain how the spectral energy distribution (SED) fitting is performed and derive the basic physical properties of galaxies in the sample. In Section 4, we measure the IRX–β relation for LBGs at $z = 3$, 4, and 5 and explain its physical origin, comparing our findings with other results from the literature. We present our conclusions in Section 5.

Throughout, magnitudes are quoted in the AB system (Oke & Gunn 1983), and we use the Chabrier (2003) stellar initial mass function (IMF). We assume a cosmology with $\Omega_m = 0.3$, $\Omega_\Lambda = 0.7$, and $H_0 = 70$ km s^{-1} Mpc^{-1}. We note that assuming the best-fitting Planck Collaboration XIII (2016) cosmology yields $\simeq 2 - 2.5$ per cent higher luminosity distances, and hence $\simeq 4 - 5$ per cent higher stellar masses and luminosities.

2 DATA

2.1 Optical & near-IR imaging

Our sample is drawn from the deep K-band image of the UKIDSS (Lawrence et al. 2007), UDS[1] data release 8 (DR8), together with the available multiwavelength photometry. The UDS is the deepest of the five UKIDSS sub-surveys (Almaini et al., in preparation), covering 0.77 deg^2 in the J, H, and K bands. The DR8 release achieves 5σ point-source depths of 24.9, 24.2, and 24.6 mag, respectively. The parent catalogue was extracted from the K-band image using SEX-TRACTOR (Bertin & Arnouts 1996). Two catalogues were constructed and merged: the first was designed to extract point sources, while the second was optimized to detect resolved galaxies (see Hartley et al. 2013 for details). The UKIDSS UDS has also been imaged by the *Canada–France–Hawaii Telescope (CFHT)* Megacam U-band (26.75 mag), Subaru Suprime-cam ($B = 27.6$, $V = 27.2$, $R = 27.0$, $i' = 27.0$, and $z' = 26.0$; Furusawa et al. 2008), and the *Spitzer* Infrared Array Camera (IRAC; Fazio et al. 2004, [3.6µm] $= 24.2$ and [4.5 µm] $= 24.0$), as a part of the UDS *Spitzer* Legacy Program (SpUDS; PI: Dunlop). To remove obvious active galactic nuclei (AGN), X-ray (Ueda et al. 2008) and radio (Simpson et al. 2006) data were used. The total coincident area of these data sets is 0.62 deg^2. All images were astrometrically aligned and multiband photometry extracted in 3-arcsec diameter apertures at the positions of K-band detections (see Simpson et al. 2012 for details), including point- spread function corrections where appropriate (Hartley et al. 2013).

2.1.1 LBG selection

The LBG selection technique relies on the fact that photons with energies higher than the rest-frame 1216 Å are almost entirely

---

absorbed by the neutral gas around the star-forming regions in the galaxy, resulting in a characteristic break that is easily identified with broad-band colours. This technique is used to identify galaxies at $z \approx 3$ using *UGR*, or *BVR*, filters (Steidel et al. 1996) but can be easily extended to higher redshifts by simply shifting the colour space to longer wavelengths, as described by Ouchi et al. (2004). In this work, we use the following selections for LBGs at $z \approx 3$ (equation 1), $z \approx 4$ (equation 2), and $z \approx 5$ (equations 3 and 4):

$$R < 27, \qquad (U - V) > 1.2,$$
$$-1.0 < (V - R) < 0.6, \quad (U - V) > 3.8(V - R) + 1.2; \tag{1}$$

$$i' < 27, \qquad (B - R) > 1.2,$$
$$(R - i') < 0.7, \quad (B - R) > 1.6(R - i') + 1.9; \tag{2}$$

$$z' < 26, \qquad (V - i') > 1.2,$$
$$(i' - z') < 0.7, \quad (V - i') > 1.8(i' - z') + 2.3; \tag{3}$$

$$z' < 26, \qquad (R - i') > 1.2,$$
$$(i' - z') < 0.7, \quad (R - i') > (i' - z') + 1.0, \tag{4}$$

where $z \approx 5$ LBGs are identified using either equations (3) or (4) in order to maximize our yield (see Ouchi et al. 2004). Note that since the parent optical catalogue is selected at K-band ($K < 24.6$), our resulting LBG sample is mass complete to a limit of $\log(M_*/M_\odot) \gtrsim 10.0$.

Photometric redshifts are determined for each source in our parent catalogue using 11 photometry bands (*UBVRi'z'JHK*[3.6][4.5]), as described in Hartley et al. (2013) and Mortlock et al. (2013), using the EAZY template-fitting code. Six SED templates were used (Brammer, van Dokkum & Coppi 2008), with the bluest template having an SMC-like extinction added. The accuracy of the photometric redshifts is assessed by comparing with the available spectroscopic data, as described in Hartley et al. (2013), with the average $|z_\mathrm{phot} - z_\mathrm{spec}|/(1 + z_\mathrm{spec}) = 0.031$.

To help eliminate low-redshift interlopers in the LBG selections, we initially enforce the minimum best-fitting (i.e. peak of the redshift probability density distribution) redshift to be $z = 2$. In the left-hand panel of Fig. 1, the normalized sum of the redshift probability distributions is shown for each redshift selection, indicating peaks at 3.35, 3.87, and 4.79. Thus, the selection criteria used here select galaxies at redshifts consistent with the target values. However, all three distributions show a minor peak at $z \approx 2.5$, indicating contamination still present in the selection. To remedy this situation, we further enforce the maximum likelihood redshifts (z_best) to be $z > 2.5$, $z > 3$, and $z > 4$ for the $z \approx 3$, $z \approx 4$, and $z \approx 5$ samples, respectively. This results in much 'cleaner' redshift probability distributions containing 3419, 699, and 60 sources at mean redshifts of 3.35, 3.87, and 4.79, respectively.

2.2 IR & sub-millimetre imaging

2.2.1 *Spitzer MIPS & Herschel SPIRE data*

We utilize mid-IR imaging from the multiband imaging photometer for *Spitzer* instrument (MIPS; Rieke et al. 2004) at 24 μm from the *Spitzer* Public Legacy Survey of the UKIDSS Ultra Deep Survey (SpUDS; PI: J. Dunlop) as described in Caputi et al. (2011) and sub-millimetre imaging from *Herschel* (Pilbratt et al. 2010), as provided by the public release of the HerMES (Oliver et al. 2012) survey undertaken with the SPIRE (Griffin et al. 2010) instrument, at 250, 350, and 500μm. The Level 2 data products from the *Herschel*

European space agency archive were retrieved, aligned, and co-added to produce maps. The de-blending procedure of the SPIRE maps is described in detail in Swinbank et al. (2014). In brief, the sources in the 24 μm catalogue were used as priors for the positions of sources contributing to the SPIRE map. The optimal sky model was found assuming 24 μm sources contribute to SPIRE sources detected at $>2\sigma$ at 250 μm and 350 μm by minimizing the residual flux density between a (PSF-convolved) sky model and the data.

Because some of the confused SPIRE sources, unassociated with our LBGs, will end up located within the SPIRE beam of the actual LBG in order to minimize the contamination in our stacks, we decided to exclude the unassociated SPIRE sources from our sample. The resulting median stacks values are summarized in Table 1.

2.2.2 *JCMT SCUBA-2 data*

We use the final, near-confusion-limited 850-μm map of the UDS from the S2CLS. Full details of the observations and data reduction are given in Geach et al. (2017), but the map spans 1 deg centred on the UDS and reaches a uniform depth of 0.9 mJy beam^{-1}. Note that this final map is a factor of 2 deeper than the map used in Coppin et al. (2015).

Similarly to SPIRE maps, we have decided to subtract all *SCUBA-2* sources with the signal-to-noise ratio of >3.5 from the 850-μm maps, which were not associated with our sample. To identify the 850-μm counterparts to our LBGs, we have used the high-resolution ALMA follow-up observations of all the *SCUBA-2* sources in the UDS field (PI:Smail), where 36 ALMA-detected LBGs were found. We note that the detailed evaluation of the ALMA-detected LBGs will be presented in Koprowski et al. (in preparation). The resulting stamps of the median stacks at each redshift bin are shown in Fig. 2, and the corresponding numbers summarized in Table 1. We find 12.0σ, 11.0σ, and 3.8σ detections in the $z \approx 3$, $z \approx 4$, and $z \approx 5$ redshift bins, respectively.

Fig. 3 shows the average radial profile of the $z \approx 3$ stack compared to the *SCUBA-2* beam (which differs slightly from a pure Gaussian). The stacked profile is indistinguishable from the shape of the beam and therefore any clustering of the sources associated with the LBGs that also contribute to the 850-μm flux density (Chary & Pope 2010; Kurczynski & Gawiser 2010; Serjeant et al. 2010) is on scales unresolved by *SCUBA-2*; i.e. below approximately 15 arcsec or 120 kpc. We ignore this potential contribution in the following analysis and consider the average sub-millimetre emission as coming from the LBG itself.

3 RESULTS

3.1 SED fitting

To fit the stacked flux densities, we use 185 SED templates compiled by Swinbank et al. (2014). These include local galaxy templates from Chary & Elbaz (2001), Rieke et al. (2009), and Draine et al. (2007) as well as high-redshift starburst galaxies from Ivison et al. (2010) and Carilli et al. (2011), with a range of dust temperatures spanning 19–60 K. With redshifts fixed at the peak values from Table 1, we find the best-fitting SEDs using a standard χ^2 minimization approach. At $z = 4.79$, only the 850-μm stacked flux density was detected at $>3\sigma$, and so here, we adopt our $z = 3.87$ best-fitting SED redshifted to $z = 4.79$ and normalized to the 850-μm flux. The fits have a consistent temperature of $T_\mathrm{d} \approx 40$ K.

We also determine the best-fitting rest-frame UV-to-milimetre model SEDs, where the UV-through-near-IR photometry and un-
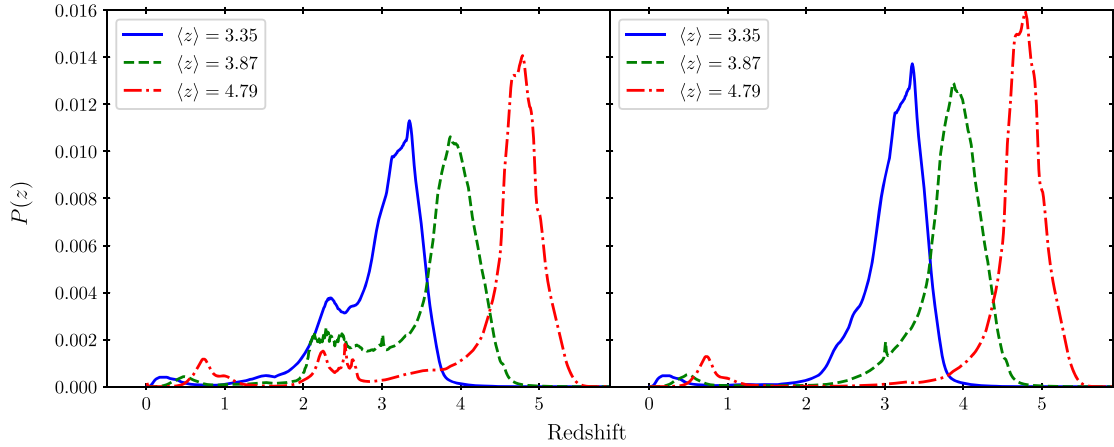
Figure 1. Redshift probability distributions with the corresponding most probable redshifts shown in the legend. *Left:* Redshift probability distributions for the LBG selection criteria from equations (1)–(4), with the additional constraint of $z > 2$ in place. It can be seen that the resulting most probable redshifts are close to the target values of 3, 4, and 5. However, the distributions show a low-redshift peak at $z \simeq 2.5$, this being the result of a number of contaminating galaxies being included using our selection criteria. *Right:* Since the $z \simeq 2.5$ sources from the left-hand panel will contaminate the inferred values of the stellar masses as well as UV slopes, we decided to introduce an additional selection criteria, where we force the best-fitting redshifts to be >2.5, >3, and >4 for the $z \sim 3$, $z \sim 4$, and $z \sim 5$ samples, respectively. This panel shows the resulting redshift probability distributions. Note that the low-redshift peaks at $z \sim 0.5$ do not result from a number of sources being found at low redshifts but rather from a small number of individual probability distributions being double-peaked (with the low-z solution having lower probability).

Table 1. Stacked IR-sub-milimetre photometry for LBGs. The columns show the most probable redshift in each bin, the number of selected LBGs, and the stacked photometry in the *Herschel* SPIRE and JCMT *SCUBA-2* 850-µm bands, with 1σ errors and detection significance in brackets.

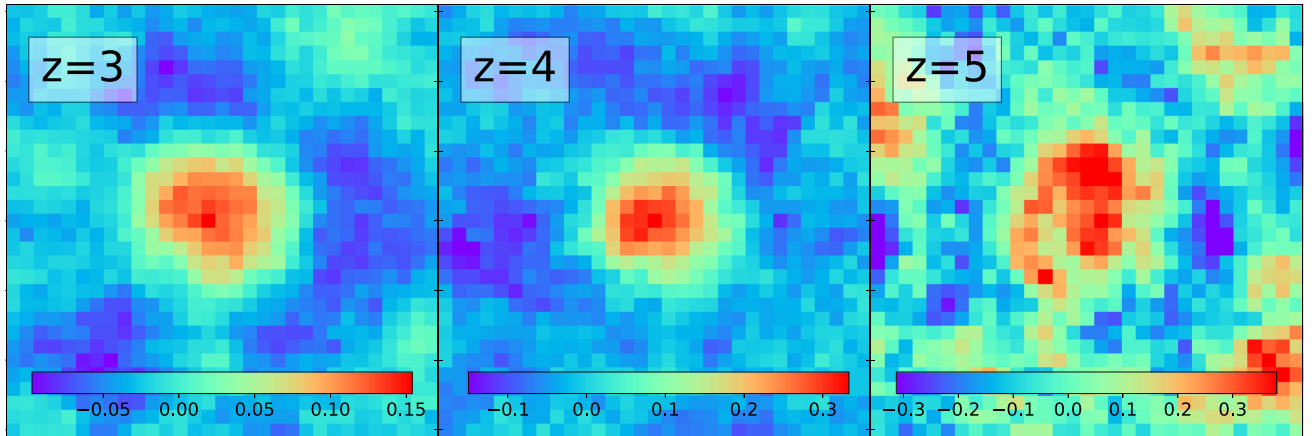| $\langle z_{phot} \rangle$	N	S_{250}/mJy	S_{350}/mJy	S_{500}/mJy	S_{850}/mJy
3.35	3439	$0.43 \pm 0.03\ (14.3\sigma)$	$0.77 \pm 0.04\ (19.3\sigma)$	$0.39 \pm 0.04\ (9.8\sigma)$	$0.12 \pm 0.01\ (12.0\sigma)$
3.87	710	$0.51 \pm 0.07\ (7.3\sigma)$	$0.77 \pm 0.09\ (8.6\sigma)$	$0.53 \pm 0.09\ (5.9\sigma)$	$0.33 \pm 0.03\ (11.0\sigma)$
4.79	60	$0.34 \pm 0.26\ (1.3\sigma)$	$0.41 \pm 0.38\ (1.1\sigma)$	$0.31 \pm 0.27\ (1.1\sigma)$	$0.30 \pm 0.08\ (3.8\sigma)$

Figure 2. 60 arcsec × 60 arcsec stamps of the median stacks at *SCUBA-2* 850-µm maps for each redshift bin, centred on the LBG positions. The resulting numbers are summarized in Table 1.

certainties are medians and median absolute deviations for all LBGs in the redshift bin. We use the 'energy balance' code CIGALE[2] (Noll et al. 2009; Serra et al. 2011), adopting the Bruzual & Charlot (2003) stellar population templates with a double-burst, exponentially declining star formation history (SFH) in which the dependence of SFR on time is

$$\Psi(t) \propto \exp(-t_1/\tau_1) + f_\mathrm{m}\exp(-t_2/\tau_2), \qquad (5)$$

with τ_1, τ_2, and the mass fraction of the late burst population, f_m, being free parameters. This allows a large variation of SFH, allowing for both single-burst and double-burst, instantaneous, exponentially declining, and continuous histories. To implement the dust attenuation, the two most extreme cases of Calzetti et al. (2000) attenuation curve and SMC-like extinction curve (Gordon et al. 2003)
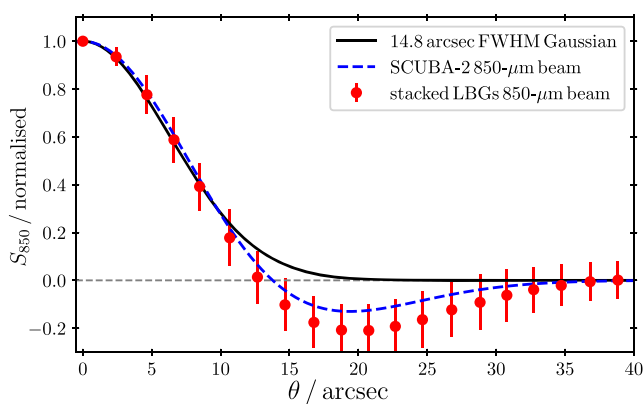
[2]http://cigale.lam.fr/

Figure 3. Light profile of the $z \approx 3$ 850-μm stack (red points) compared with the *SCUBA-2* 850-μm beam (dashed blue line) of Geach et al. (2017) and a 14.8 arcsec FWHM Gaussian (black solid curve). The stacked profile is consistent with the beam and therefore any contribution from clustering of associated sources must be on scales below 15 arcsec, if present at all.

were used. Finally, the thermal dust emission was modelled with the modified grey bodies of Casey (2012), where the mid-infrared power-law slope and dust- emissivity index are fixed at 2.6 and 1.6, respectively, while the temperature is allowed to vary between 20 and 80 K.[3] The best-fitting SEDs are plotted in Fig. 4 as black curves. Since CIGALE uses energy balance, the unattenuated stellar emission SEDs can be estimated for each of the adopted attenuation/extinction curves, which we show in Fig. 4 as blue solid and brown dashed lines, for the Calzetti et al. (2000) attenuation and SMC-like extinction curves, respectively.

3.2 UV & IR luminosities and stellar masses

The CIGALE fits described above are used to estimate the average stellar mass of each sample. As noted by Dunlop (2011), the use of a multicomponent SFH generally leads to more accurate values of stellar mass than the use of a single SFH. This is due to the fact that in a single-burst scenario the entire stellar population must be young in order to reproduce the UV emission, thus the less massive but more abundant old stars are often not properly accounted for (see also Michałowski et al. 2012, 2014). The stellar mass distributions and corresponding mean values for each redshift bin are shown in Fig. 5, with the numbers summarized in Table 2. The average stellar mass increases with redshift, which is a simple consequence of the NIR selection limit for our parent catalogue (Section 2.1), as shown in Fig. 6. For the same reason, our *K*-band-limited sample is only complete to a stellar mass limit of $\log(M_*/M_\odot) \gtrsim 10.0$ (see Fig. 6).

The UV luminosity is defined here as $L_{UV} \equiv \nu_{1600}L_{1600}$, where the luminosity density at rest-frame 1600 Å, L_{1600}, is determined from the best-fitting SED. The luminosity distributions are shown in the right-hand panel of Fig. 5, with the mean values summarized in Table 2. Again, L_{UV} is increasing with redshift, which, as in the case of the stellar mass, is a result of the fixed optical flux limits

---

[3]Note, that the dust temperature in the Casey (2012) models is an effective temperature, which is numerically higher than the temperature normally quoted in the literature, T_d, corresponding to the peak of the thermal infrared emission (see Fig. 2 in Casey 2012).

in the LBG selection. While the difference between $z = 3.35$ and $z = 3.87$ is small ($R < 27$ and $i' < 27$ from equations 1 and 2, respectively), the UV luminosity for $z = 4.79$ is significantly higher because the corresponding rest-frame UV imaging is shallower ($z' < 26$, equations 3 and 4).

Finally, total IR luminosities are determined by integrating under the best-fitting IR SED between rest-frame 8 and 1000 μm (Table 2). Again, average L_{IR} increases with redshift, which is most likely linked to the increase in stellar mass rather than a real evolutionary trend.

4 ANALYSIS AND DISCUSSION

4.1 IRX–β relation

4.1.1 UV slopes

Several different techniques have been used in the literature to measure the UV slope, β (see Rogers, McLure & Dunlop 2013 for a review). The original work of Meurer et al. (1999) fitted a simple power-law to the 10 continuum bands listed by Calzetti, Kinney & Storchi-Bergmann (1994) in the rest-frame range of ~1250–2500 Å. In most cases, however, only a few bands are available in that range, introducing uncertainty on β. In addition, the possible existence of the 2175-Å feature in the dust attenuation curve can potentially impact the inferred values of the photometry-based UV slopes, driving up scatter in β. As shown by McLure et al. (2018) and explained further next, this scatter is significant enough to cause a bias that serves to flatten the IRX–β relation. To try to minimize these effects, we measure β by fitting a power-law to the best-fitting SED over a rest-frame range of 1250–2500 Å rather than the photometry directly.

4.1.2 Stacking IRX

To measure the average IRX $\equiv L_{IR}/L_{UV}$, we first bin the sample in β. We do not a priori know how L_{IR} couples with L_{UV}, so we cannot assume that the ⟨IRX⟩ in each β bin is simply equal to ⟨L_{IR}⟩/⟨L_{UV}⟩. Therefore, we cannot stack the 850-μm flux densities (i.e. L_{IR}) and divide by the mean L_{UV}. Instead, we follow Bourne et al. (2017) by assuming that ⟨IRX⟩ $\equiv$ ⟨L_{IR}/L_{UV}⟩, stacking individual values of IRX, which is more directly comparable to individually detected galaxies in the IR (eg. Capak et al. 2015; Koprowski et al. 2016). We find the individual values of L_{IR} assuming all LBGs are described by the average best-fitting template and normalize this to the observed 850-μm flux density at the position of each galaxy. Uncertainties on individual L_{IR} are estimated from the same measurement in noise-only maps at 850 μm using the same scaling factor. The results are presented in Fig. 7 and Table 3.

We stress that the individual values of IRX and β have been calculated independently, and that we did not use the energy balance available in CIGALE. The L_{IR} for each LBG was found from the best-fitting empirical dust-emission SEDs (red curves in Fig. 4), while the L_{UV} and β were determined from the best-fitting SED to the rest-frame UV-NIR photometry available for each of the sources in our sample. We also note that the choice of the attenuation/extinction curve only affects the shape of the resulting *intrinsic* stellar SEDs (blue solid and brown dashed curves in Fig. 4) and has no effect on the inferred values of the observed UV slopes.
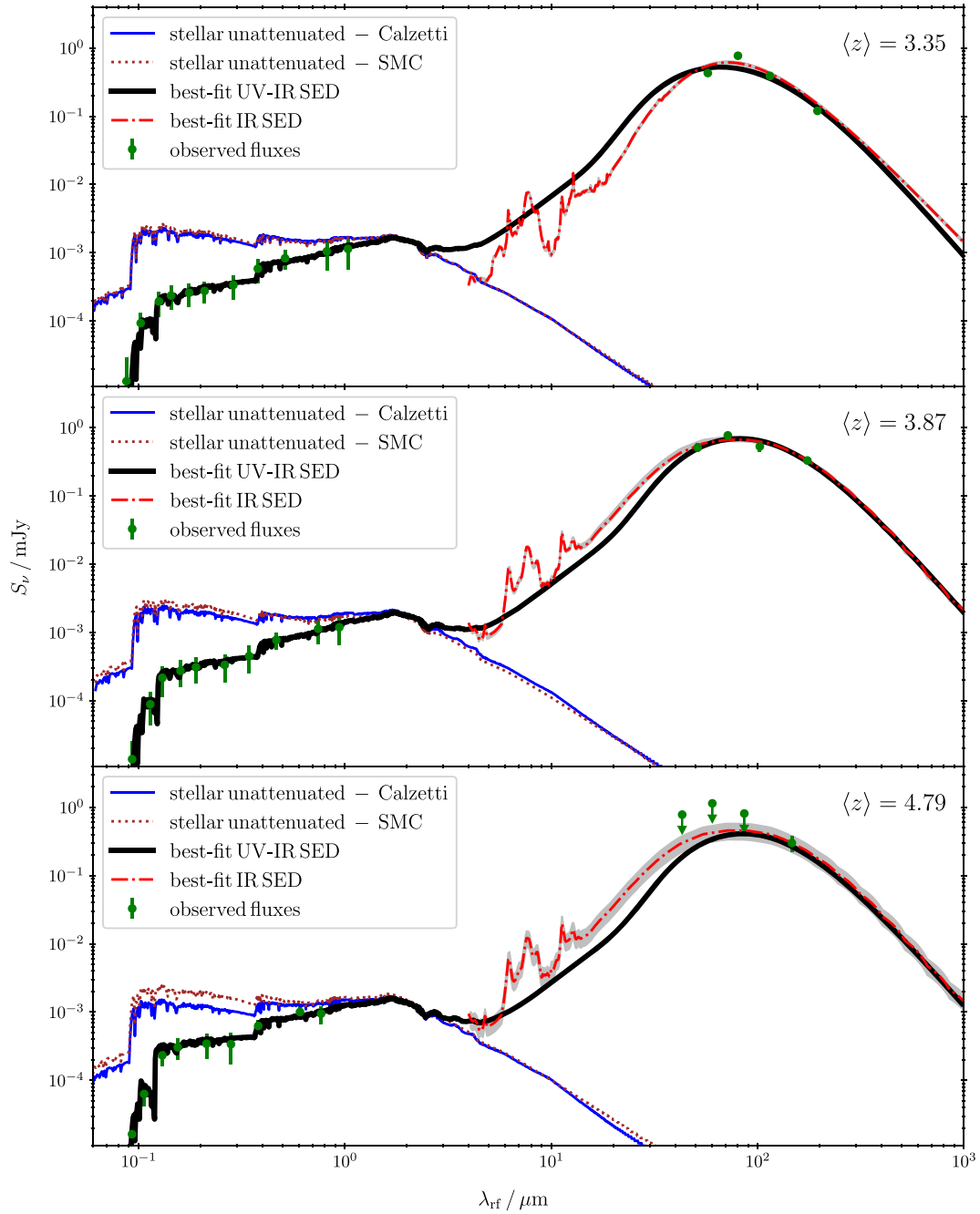
Figure 4. Best-fitting SEDs at rest-frame wavelengths for the stacked results in each redshift bin. The IR photometry comes from stacking LBGs in *Herschel* SPIRE and JCMT *SCUBA-2* 850-μm bands, while the rest-frame UV-NIR photometry points are median values from all the LBGs in a given redshift bin, with the errors being median absolute deviations. The red curves (used in the calculations of L_{IR}) are best-fitting empirical IR SEDs of Swinbank et al. (2014) found using an χ^2 minimization method. In addition, we plot in black the best-fitting rest-frame UV-milimetre SEDs found using CIGALE, where Bruzual & Charlot (2003) stellar population templates, Chabrier (2003) IMF, and the thermal-dust-emission model of Casey (2012) were adopted (see Section 3.1 for details). For the dust attenuation, the two most extreme cases of Calzetti et al. (2000) and SMC (Gordon et al. 2003) were used, with the corresponding unattenuated stellar emission SED shown with blue solid and brown dashed lines, respectively.

4.1.3 Functional form of IRX–β relation

We adopt a functional form of IRX from Meurer et al. (1999)

$$IRX = (10^{0.4 A_{1600}} - 1) \times B, \qquad (6)$$

where A_{1600} is the attenuation at the rest-frame 1600 Å in magnitudes and B is the ratio of two bolometric corrections
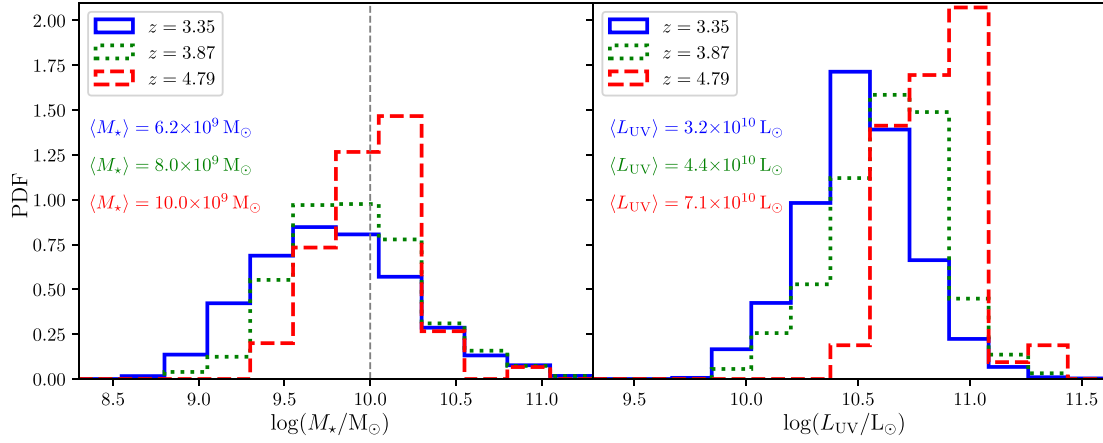
$$B = \frac{BC(1600)}{BC(FIR)}. \qquad (7)$$

Figure 5. *Left:* Histogram of stellar masses for each redshift bin found from the best-fitting rest-frame UV-NIR SEDs (see Section 3.2 for details). It can be seen that the masses increase with redshift, which is a consequence of the selection limit for our parent catalogue of $K < 24.6$. Since we can treat K-band as a rough proxy for the stellar mass (see Fig. 6), we expect the average mass to increase with redshift due to the positive K-correction in this band. The grey dashed line marks the mass limit down to which our LBG sample is complete. This is a consequence of our parent optical catalogue being selected at K-band (see also Fig. 6). *Right:* Histogram of the UV luminosities for each redshift bin in this work. As in the case of the stellar masses, the UV luminosities tend to increase with redshift. Again, this is caused by the depth of our parent catalogue in the rest-frame UV bands.

Table 2. Physical properties for LBGs. The stellar masses and UV luminosities are mean values in each bin (see Fig. 5), with the errors being standard deviations rather than the errors on the mean (gives indication of the scatter). The IR luminosities are found by integrating the best-fitting empirical IR templates (red curves in Fig. 4) between 8 and 1000 μm.

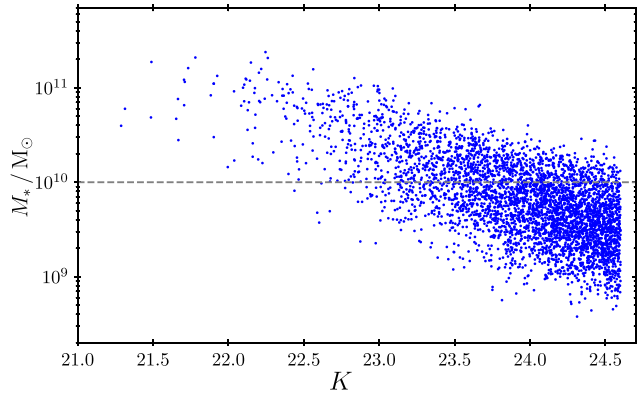| $\langle z \rangle$	$\log(M_*/M_\odot)$	$\log(L_{\mathrm{UV}}/L_\odot)$	$\log(L_{\mathrm{IR}}/L_\odot)$
3.35	9.78 ± 0.45	10.51 ± 0.25	$11.37^{+0.02}_{-0.02}$
3.87	9.89 ± 0.38	10.65 ± 0.27	$11.61^{+0.04}_{-0.02}$
4.79	10.00 ± 0.27	10.85 ± 0.17	$11.59^{+0.10}_{-0.13}$

Figure 6. Stellar mass as a function of the K-band magnitude for the whole LBG sample used in this work. It can be seen that the K-band can be treated as a very rough proxy of the stellar mass. Applying a K-band cut of 24.6 (Section 2.1) at all three redshift bins causes slightly higher stellar masses to be selected at higher redshift bins due to the positive K-correction (see Fig. 5 and Table 2). The dashed grey line marks the mass-completeness limit, being the consequence of our parent optical catalogue being selected at K-band.

The original Meurer et al. (1999) relation was defined as IRX $\equiv L_{\mathrm{FIR}}/L_{\mathrm{UV}}$, where

$$L_{\mathrm{FIR}} = 1.25(L_{60} + L_{100}), \qquad (8)$$

with L_{60} and L_{100} are the luminosities measured by *IRAS* at 60 and 100 μm. To correct from L_{FIR} to total bolometric IR luminosity, the BC(FIR) correction was needed. Here, we defined IRX as $L_{\mathrm{IR}}/L_{\mathrm{UV}}$, so the IR bolometric correction factor, BC(FIR), is by definition equal to unity. The UV bolometric correction, BC(1600), converts between all the stellar light available to heat the dust and the intrinsic F_{1600} measured at the rest-frame 1600 Å. This can be calculated once the intrinsic stellar-emission SED is known by integrating between the 912 Å (Lyman limit) and infinity. As explained above, we consider the two most extreme cases of a Calzetti et al. (2000) attenuation curve and an SMC-like extinction curve (Gordon et al. 2003).

To find the average intrinsic stellar emission SED corresponding to each of the attenuation/extinction curves, we used the energy balance feature of CIGALE, where the amount of the stellar light attenuated by dust is assumed to be equal to the light re-emitted in the IR (Table 2). The resulting UV bolometric corrections, BC(1600), and the intrinsic UV slopes, β_{int}, for both attenuation/extinction curves for each redshift bin are given in Table 4.

The attenuation at 1600 Å, A_{1600} from equation (6), can be described as

$$A_{1600} = \frac{\delta A_{1600}}{\delta \beta}(\beta_{\mathrm{obs}} - \beta_{\mathrm{int}}), \qquad (9)$$

where $\delta A_{1600}/\delta \beta$ is the slope of the reddening law, and β_{obs} and β_{int} are the observed and the intrinsic UV slopes, respectively. To find the slope of the reddening law for the Calzetti- and SMC-like curves, we redden an intrinsic (dust unattenuated) stellar SED (blue curves in Fig. 4) in small steps and calculate the amount of the attenuated stellar light. This is then equated with the energy re-emitted in the IR by dust. The results of this exercise are depicted in Fig. 8, where we find slopes of 2.1 for the Calzetti- and 0.9 for the SMC-like dust.

The resulting functional forms of the IRX–β relations (equations 6, 7, and 9) for each attenuation/extinction curve in each redshift bin are summarized in Table 4 and plotted in Fig. 7. It is clear from Fig. 7, that our data are consistent with Calzetti-like dust attenuation (similar to McLure et al. 2018 find at $z \sim 3$), and that there is no significant evolution of the IRX–β relation with redshift, as found for the sub-milimetre bright *SCUBA-2* galaxies by Bourne
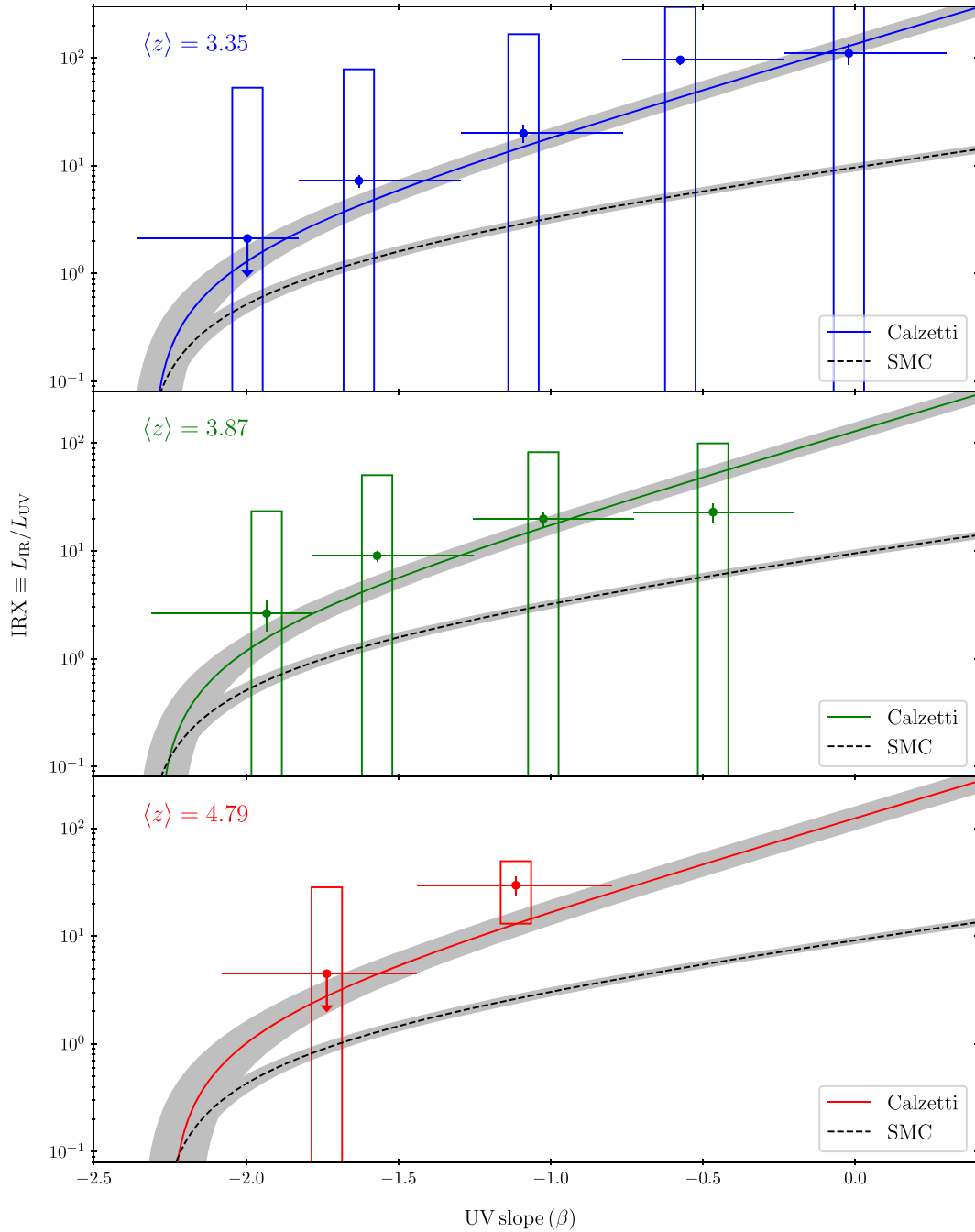
Figure 7. IRX–β relation for each redshift bin studied in this work. UV slopes were determined from the best-fitting SEDs to the rest-frame UV-NIR data only. The coloured points with error bars are the stacked values (Table 3), where we average the IRX values in each β and redshift bin (see Section 4.1.2 for details). The bars on β merely represent the widths of a given bin, while the values and errors on IRX are medians and median absolute deviations divided by the square root of the sample size, respectively (with 3σ upper limits). The coloured rectangles depict the 1σ scatter in the individual values of the IRX in each β bin. The curves depict the functional forms of the IRX–β relation (Table 4), derived at each redshift bin for Calzetti- and SMC-like dust (see Section 4.1.3 for details). It is clear from this plot that our data are consistent with the Calzetti-like attenuation curve and also that there is no obvious redshift evolution of the relation.

et al. (2017). It is also clear from Fig. 8 that galaxies following a given IRX–β relation have on average similar intrinsic UV slopes with similar corresponding stellar populations, consistent with the models of Narayanan et al. (2018), Popping, Puglisi & Norman (2017), and Safarzadeh, Hayward & Ferguson (2017).

4.2 Comparison with recent studies

In Fig. 9, we compare our $z = 3.35$ results with others works: Heinis et al. (2013), Álvarez-Márquez et al. (2016), Reddy et al. (2018), and McLure et al. (2018). Solid and dashed black lines represent the functional forms of the IRX–β relation for Calzetti-like atten-

Table 3. Stacking results for our LBG sample. In each β bin, the value of the UV slope is the unweighted average, and the error bars correspond to the width of a given bin. A total number of LBGs in each β bin are given, and the median IRX values with the errors being median absolute deviations are divided by the square root of the sample size. The stellar mass in each stellar mass bin is the mean with the error being the standard error on the mean. The lowest mass bin upper limit is the only mass-incomplete data point (see Fig. 6).

Sample	N	⟨IRX⟩
β bins :		
z = 3.35		
β = −2.00	1523	<2.11
β = −1.63	1422	7.25 ± 0.94
β = −1.09	315	19.97 ± 3.71
β = −0.57	115	95.70 ± 8.81
β = −0.02	43	110.21 ± 23.92
z = 3.87	−	−
β = −1.93	228	2.63 ± 0.83
β = −1.57	353	9.02 ± 0.97
β = −1.02	85	19.85 ± 2.94
β = −0.47	31	22.92 ± 4.74
z = 4.79	−	−
β = −1.74	50	<4.47
β = −1.11	7	29.58 ± 5.83
M_∗ bins :	−	−
$\log(M_*/M_\odot) = 9.47 \pm 0.13$	1339	<2.30
$\log(M_*/M_\odot) = 9.90 \pm 0.13$	1635	4.71 ± 0.67
$\log(M_*/M_\odot) = 10.33 \pm 0.13$	722	20.39 ± 1.30
$\log(M_*/M_\odot) = 10.81 \pm 0.13$	176	34.93 ± 3.73

Table 4. Functional forms of the IRX–β relation for Calzetti-like attenuation and SMC-like extinction curves (see Section 4.1.3 for details) plotted in Fig. 7.

z	IRX	A_{1600}
	Calzetti-like attenuation curve	
3.35	$(1.56 \pm 0.07) \times (10^{0.4A_{1600}} - 1)$	$2.10(\beta + (2.31 \pm 0.07))$
3.87	$(1.56 \pm 0.06) \times (10^{0.4A_{1600}} - 1)$	$2.10(\beta + (2.29 \pm 0.07))$
4.79	$(1.62 \pm 0.10) \times (10^{0.4A_{1600}} - 1)$	$2.10(\beta + (2.25 \pm 0.09))$
	SMC-like extinction curve	
3.35	$(1.54 \pm 0.05) \times (10^{0.4A_{1600}} - 1)$	$0.92(\beta + (2.34 \pm 0.04))$
3.87	$(1.52 \pm 0.04) \times (10^{0.4A_{1600}} - 1)$	$0.92(\beta + (2.34 \pm 0.04))$
4.79	$(1.53 \pm 0.04) \times (10^{0.4A_{1600}} - 1)$	$0.92(\beta + (2.29 \pm 0.04))$

Figure 8. Infrared excess as a function of the observed UV slope for Calzetti-like attenuation and SMC-like extinction curves. The points represent the results of the simulations, wherein the unattenuated stellar emission SED was reddened using both, the Calzetti-like attenuation and SMC-like extinction curves in small steps. In each step, the resulting IRX value was determined based on the balance between the energy attenuated in the rest-frame UV and re-emitted in the IR. The solid lines are the best-fitting functional forms (equation 6), with the resulting slopes of 2.1 and 0.92 for the Calzetti- and SMC-like dust, respectively (see Section 4.1.3 for details).

To investigate the effects of the scatter of the photometry-based UV slopes about their real values on the resulting shape of the IRX–β relation, we have re-stacked our z = 3.35 data. To estimate the UV slope for each galaxy, we fit a simple power-law to the photometry available in the rest-frame range of 1250–2500 Å and then stack the IRX in the same β bins as in Section 4.1.2. The results are shown in Fig. 9 as white circles. It can be seen that at the red end, IRX values are suppressed, effectively flattening to relation, and pushing towards the SMC-like curve. This is because, with our present data, we only have three continuum bands in the rest-frame range of 1250–2500 Å, resulting in larger errors on β and therefore more scatter in individual β bins. Using power-law fits to the corresponding rest-frame UV range in the best-fitting SEDs, using all 11 bands of observational data (even if this is not in the nominal range for a direct estimate of β), significantly reduces this scatter.

Another approach, taken by McLure et al. (2018), is to bin the sample in stellar mass. This is motivated by the growing consensus that it is the total stellar mass that influences the amount of the dust extinction (Heinis et al. 2013; Álvarez-Márquez et al. 2016; Dunlop et al. 2017; Reddy et al. 2018). We show the stellar mass-binned results of McLure et al. (2018) in Fig. 9 as red circles. It clearly shows, consistent with this work, that z ∼ 3 LBGs are affected by dust extinction characteristic of the Calzetti et al. (2000) law. With M_* being a more fundamental parameter, often the dependence of IRX on M_* is determined, instead of UV slope. To this end, we stack the z ≈ 3 sample in bins of M_*. The results are shown in Fig. 10 as black circles, with a best-fitting power-law curve of

$$\log(\text{IRX}) = (0.87 \pm 0.10) \times \log(M_*/10^{10}M_\odot) + (0.98 \pm 0.04),$$
(10)

and the grey area depicting 1σ uncertainties. Our results are in excellent agreement with McLure et al. (2018), who find a virtually identical form, with a slope of 0.85 ± 0.05 and zero-point of 0.99 ± 0.03. We also compare other results in the literature corresponding to the data from Fig. 9. One can see that the inconsistencies between different works are much smaller, most likely because the

uation and SMC-like extinction curves from Table 4. Systematic differences can be immediately noted. McLure et al. (2018) and this work are consistent with Calzetti-like dust, while other work is intermediate between the Calzetti- and SMC-like curves. A potential reason for this inconsistency, pointed out by McLure et al. (2018) and noted earlier, is the relatively large uncertainty associated with the determination of the photometry-based values for UV slopes. Since the reddest β bins are populated by very few sources, a small number of overestimated UV slopes can cause an apparent drop in IRX, pushing values towards the SMC-like curve.
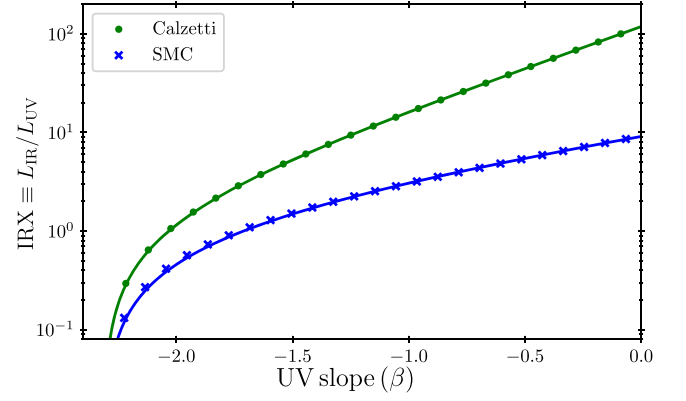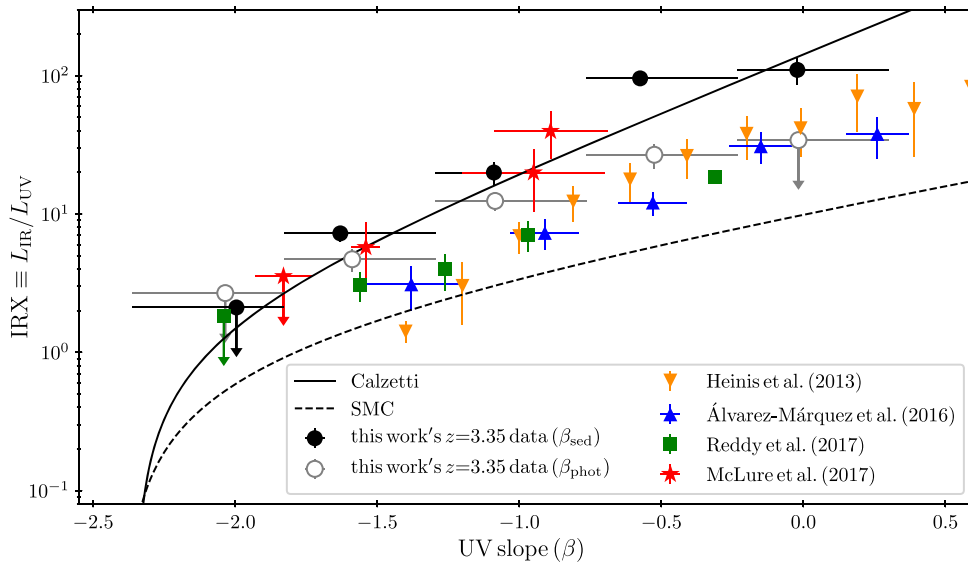
Figure 9. IRX–β relation for $z \sim 3$ LBGs for this work's sample (black circles) compared with some of the recent literature results (Heinis et al. 2013; Álvarez-Márquez et al. 2016; Reddy et al. 2018; McLure et al. 2018). The black solid and dashed lines represent the Calzetti- and SMC-like dust curves from Table 4. It is clear, while ours and McLure et al. (2018) data are consistent with the Calzetti-like dust, others seem to be lying between two dust curves. As shown by McLure et al. (2018), this is caused by the uncertainties in the inferred values of the photometry-based UV slopes. We confirm this by including the data with β's determined from the best-fitting power laws to the rest-frame 1250–2500 Å photometry (white circles). One can clearly see that significantly larger errors on the photometry-based values of β flatten the slope of the corresponding IRX–β relation (see Section 4.2 for details).
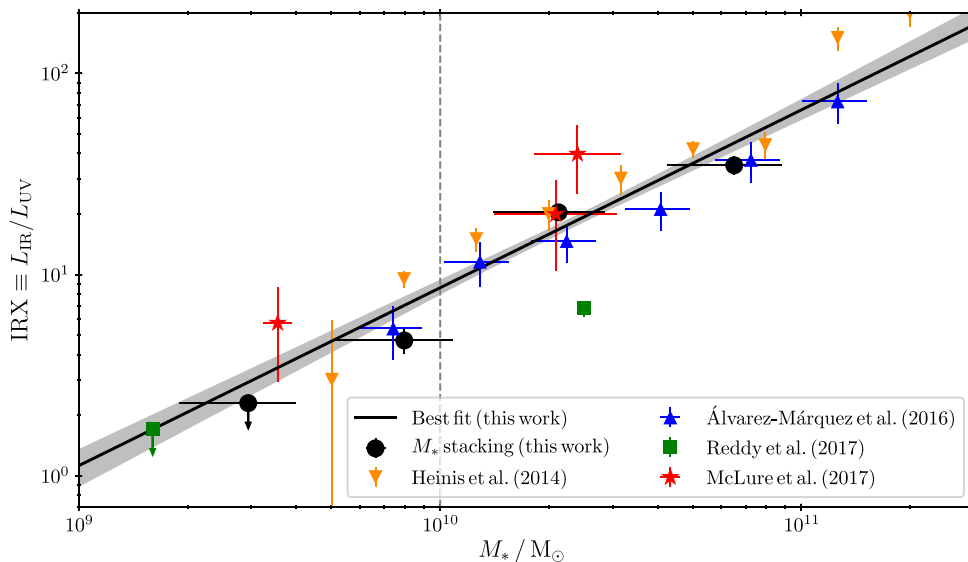

Figure 10. IRX–M_* relation for our $z \sim 3$ LBGs compared with recent literature results (Heinis et al. 2013; Álvarez-Márquez et al. 2016; McLure et al. 2018; Reddy et al. 2018) from Fig. 9. It is clear that the rather striking systematic inconsistencies from Fig. 9 now appear significantly decreased. This further confirms that the scatter in Fig. 9 is mainly driven by different techniques of determining β. This is because in the IRX–M_* relation, stellar masses are determined from the best-fitting SEDs, with the corresponding errors of a very similar order (see Section 4.2 for details). The dashed line represents the mass limit down to which our LBG sample is complete. The lowest mass upper limit is therefore the only mass-incomplete data point.

stellar masses are in all cases determined from the best-fitting SEDs well sampled with photometry.

5   CONCLUSIONS

We have extended the work of Coppin et al. (2015) to improve on and calibrate the IRX–β relation at $z \simeq 3$–5 using 4178 LBGs, stellar mass complete down to a limit of $\log(M_*/M_\odot) \gtrsim 10.0$. We are able to determine the average total IR luminosity by stacking galaxies

in deep *SCUBA-2* 850 μm and SPIRE 250–500 μm imaging. By evaluating the observed UV slope, β, and emergent UV luminosity, we investigate the infrared excess, IRX, as a function of observed UV slope and stellar mass, deriving functional forms. We conclude the following:

(i) $3 < z < 5$ LBGs are consistent with the Calzetti et al. (2000) attenuation law, consistent with the findings of McLure et al. (2018), Cullen et al. (2017), and Cullen et al. (2018) at $z \sim 3$, now extended

to $z \sim 5$. This describes a scenario, where dust and stars are 'well mixed,' on average. In addition, similarly to Bourne et al. (2017), we find no significant redshift evolution in the IRX–β over $z \approx 3$–5.

(ii) The IRX–β relationship for LBGs in our sample is characteristic of galaxies with similar stellar population ages, corresponding to similar intrinsic UV slopes ($\beta_{intr} \sim -2.3$), such that the observed value of β is entirely driven by dust obscuration. In turn, this increases the corresponding IR luminosity, and hence the IRX. This picture is consistent with the theoretical work of Narayanan et al. (2018), Popping et al. (2017), and Safarzadeh et al. (2017).

(iii) Comparing our results with the recent literature findings of Heinis et al. (2013), Álvarez-Márquez et al. (2016), Reddy et al. (2018), and McLure et al. (2018), we find some inconsistencies, where some papers have found significantly lower IRX values for a given β, implying a more 'SMC-like' relation. We have confirmed that these inconsistencies are driven by scatter in measured values of β from limited photometry that serves to artificially flatten IRX–β. The scatter is significantly reduced by determining β from full SED fits.

(iv) Stacking IRX in bins of stellar mass, instead of as a function of β, results in a much more consistent picture. There is a tight IRX–M_* relation in which dust-reprocessed stellar emission scales nearly linearly with stellar mass. There is much better consistency across different works in this parameter space, likely due to the full SED fitting used to derive stellar masses, reducing relative uncertainties. We agree that the IRX–$M_\star$ relationship is probably a far better proxy for correcting observed UV luminosities to total SFRs, provided an accurate handle on $M_\star$, and also gives clues as to the physical driver of dust-obscured star formation in high-redshift galaxies.

ACKNOWLEDGEMENTS

REFERENCES

Baugh C. M., Lacey C. G., Frenk C. S., Granato G. L., Silva L., Bressan A., Benson A. J., Cole S., 2005, MNRAS, 356, 1191

Bertin E., Arnouts S., 1996, A&AS, 117, 393

Bian F. et al., 2013, ApJ, 774, 28

Blaizot J., Guiderdoni B., Devriendt J. E. G., Bouchet F. R., Hatton S. J., Stoehr F., 2004, MNRAS, 352, 571

Bourne N. et al., 2017, MNRAS, 467, 1360

Bouwens R. J. et al., 2016, ApJ, 833, 72

Brammer G. B., van Dokkum P. G., Coppi P., 2008, ApJ, 686, 1503

Bruzual G., Charlot S., 2003, MNRAS, 344, 1000

Calzetti D., Kinney A. L., Storchi-Bergmann T., 1994, ApJ, 429, 582

Calzetti D., Armus L., Bohlin R. C., Kinney A. L., Koornneef J., Storchi-Bergmann T., 2000, ApJ, 533, 682

Capak P. L. et al., 2015, Nature, 522, 455

Caputi K. I., Cirasuolo M., Dunlop J. S., McLure R. J., Farrah D., Almaini O., 2011, MNRAS, 413, 162

Carilli C. L., Hodge J., Walter F., Riechers D., Daddi E., Dannerbauer H., Morrison G. E., 2011, ApJ, 739, L33

Casey C. M. et al., 2014, ApJ, 796, 95

Casey C. M., 2012, MNRAS, 425, 3094

Chabrier G., 2003, ApJ, 586, L133

Chapman S. C. et al., 2000, MNRAS, 319, 318

Chapman S. C., Casey C. M., 2009, MNRAS, 398, 1615

Chary R., Elbaz D., 2001, ApJ, 556, 562

Chary R.-R., Pope A., 2010, preprint (arXiv:1003.1731)

Coppin K. E. K. et al., 2015, MNRAS, 446, 1293

Cullen F. et al., 2018, MNRAS, 476, 3218

Cullen F., McLure R. J., Khochfar S., Dunlop J. S., Dalla Vecchia C., 2017, MNRAS, 470, 3006

Dole H. et al., 2006, A&A, 451, 417

Draine B. T. et al., 2007, ApJ, 663, 866

Dunlop J. S. et al., 2017, MNRAS, 466, 861

Dunlop J. S., 2011, in Wang W., Lu J., Luo Z., Yang Z., Hua H., Chen Z., eds, ASP Conf. Ser. Vol. 446, Galaxy Evolution: Infrared to Millimeter Wavelength Perspective. Astron. Soc. Pac., San Francisco, p. 209

Fazio G. G. et al., 2004, ApJS, 154, 10

Fudamoto Y. et al., 2017, MNRAS, 472, 483

Furusawa H. et al., 2008, ApJS, 176, 1

Geach J. E. et al., 2017, MNRAS, 465, 1789

Giavalisco M., 2002, ARA&A, 40, 579

Gordon K. D., Clayton G. C., Misselt K. A., Landolt A. U., Wolff M. J., 2003, ApJ, 594, 279

Griffin M. J. et al., 2010, A&A, 518, L3

Hartley W. G. et al., 2013, MNRAS, 431, 3045

Heinis S. et al., 2013, MNRAS, 429, 1113

Ivison R. J. et al., 2010, MNRAS, 402, 245

Kennicutt R. C., Evans N. J., 2012, ARA&A, 50, 531

Koprowski M. P. et al., 2016, ApJ, 828, L21

Kurczynski P., Gawiser E., 2010, AJ, 139, 1592

Lawrence A. et al., 2007, MNRAS, 379, 1599

Lo Faro B., Monaco P., Vanzella E., Fontanot F., Silva L., Cristiani S., 2009, MNRAS, 399, 827

Madau P., Dickinson M., 2014, ARA&A, 52, 415

Madau P., Ferguson H. C., Dickinson M. E., Giavalisco M., Steidel C. C., Fruchter A., 1996, MNRAS, 283, 1388

Magdis G. E., Rigopoulou D., Huang J.-S., Fazio G. G., Willner S. P., Ashby M. L. N., 2008, MNRAS, 386, 11

Magdis G. E., Rigopoulou D., Huang J.-S., Fazio G. G., 2010, MNRAS, 401, 1521

McLure R. J. et al., 2018, MNRAS, 476, 3991

Meurer G. R., Heckman T. M., Calzetti D., 1999, ApJ, 521, 64

Michałowski M. J., Dunlop J. S., Cirasuolo M., Hjorth J., Hayward C. C., Watson D., 2012, A&A, 541, A85

Michałowski M. J., Hayward C. C., Dunlop J. S., Bruce V. A., Cirasuolo M., Cullen F., Hernquist L., 2014, A&A, 571, A75

Mortlock A. et al., 2013, MNRAS, 433, 1185

Narayanan D., Davé R., Johnson B. D., Thompson R., Conroy C., Geach J., 2018, MNRAS, 474, 1718

Noll S., Burgarella D., Giovannoli E., Buat V., Marcillac D., Muñoz-Mateos J. C., 2009, A&A, 507, 1793

Oke J. B., Gunn J. E., 1983, ApJ, 266, 713

Oliver S. J. et al., 2012, MNRAS, 424, 1614

Oteo I. et al., 2013, A&A, 554, L3

Ouchi M. et al., 2004, ApJ, 611, 660

Overzier R. A. et al., 2011, ApJ, 726, L7

Pentericci L., Grazian A., Scarlata C., Fontana A., Castellano M., Giallongo E., Vanzella E., 2010, A&A, 514, A64

Pilbratt G. L. et al., 2010, A&A, 518, L1

Planck Collaboration XIII, 2016, A&A, 594, A13

Popping G., Puglisi A., Norman C. A., 2017, MNRAS, 472, 2315

Reddy N. A. et al., 2018, ApJ, 853, 56

Reddy N. A., Steidel C. C., 2009, ApJ, 692, 778

Reddy N. A., Steidel C. C., Fadda D., Yan L., Pettini M., Shapley A. E., Erb D. K., Adelberger K. L., 2006, ApJ, 644, 792

Rieke G. H. et al., 2004, ApJS, 154, 25

Rieke G. H., Alonso-Herrero A., Weiner B. J., Pérez-González P. G., Blaylock M., Donley J. L., Marcillac D., 2009, ApJ, 692, 556

Rigopoulou D. et al., 2006, ApJ, 648, 81

Rigopoulou D. et al., 2010, MNRAS, 409, L7

Rogers A. B., McLure R. J., Dunlop J. S., 2013, MNRAS, 429, 2456

Safarzadeh M., Hayward C. C., Ferguson H. C., 2017, ApJ, 840, 15

Sawicki M., Yee H. K. C., 1998, AJ, 115, 1329

Scoville N. et al., 2016, ApJ, 820, 83

Serjeant S. et al., 2010, A&A, 518, L7

Serra P., Amblard A., Temi P., Burgarella D., Giovannoli E., Buat V., Noll S., Im S., 2011, ApJ, 740, 22

Shapley A. E., Steidel C. C., Adelberger K. L., Dickinson M., Giavalisco M., Pettini M., 2001, ApJ, 562, 95

Shapley A. E., Steidel C. C., Erb D. K., Reddy N. A., Adelberger K. L., Pettini M., Barmby P., Huang J., 2005, ApJ, 626, 698

Simpson C. et al., 2006, MNRAS, 372, 741

Simpson C. et al., 2012, MNRAS, 421, 3060

Somerville R. S., Primack J. R., Faber S. M., 2001, MNRAS, 320, 504

Stark D. P., Ellis R. S., Bunker A., Bundy K., Targett T., Benson A., Lacy M., 2009, ApJ, 697, 1493

Steidel C. C., Giavalisco M., Pettini M., Dickinson M., Adelberger K. L., 1996, ApJ, 462, L17

Swinbank A. M. et al., 2014, MNRAS, 438, 1267

Ueda Y. et al., 2008, ApJS, 179, 124

Verma A., Lehnert M. D., Förster Schreiber N. M., Bremer M. N., Douglas L., 2007, MNRAS, 377, 1024

Álvarez-Márquez J. et al., 2016, A&A, 587, A122

This paper has been typeset from a TEX/LATEX file prepared by the author.